Investigation on the Fracture Behavior of Shape Memory Alloy NiTi

J.H. CHEN, W. SUN, and G.Z. WANG

This work investigates the fracture behavior of shape memory alloy NiTi (50.7 at. pct Ni) at room temperature. Macroscopic mechanical tests, microscopic *in situ* observations of tensile fracture processes by scanning electron microscopy (SEM), and detailed analyses of fracture surfaces were carried out. The results reveal that specimens with different thicknesses show various shape memory effects and superelasticities. The main crack with a quasi-cleavage mode that combines cleavage with ductile tearing is initiated at the notch tip and is stress-control-propagated in line with the direction of the maximum normal stress. The microstructure has little effect on the direction of crack propagation, but coarser substructures show lower resistance to the crack propagation. In specimens with various types of notches, various notch acuities present different effects on the crack initiation and propagation and result in different fracture behaviors.

I. INTRODUCTION

IN addition to shape memory effect, NiTi alloy has properties such as repeatability of mechanic behaviors, wear resistance, corrosion resistance, and biocompatibility. These superior properties make NiTi alloys one of the most commercially successful shape memory alloys used for nonvascular and vascular stents in biomedical applications and for the fixation of damaged bone.[1,2,3] However, as an intermetallic compound, it is rather brittle and rare accidents have been reported of broken NiTi parts in the human body. Therefore, the fracture behavior is a subject to be investigated in order to improve this alloy. In past decades, most work for this alloy had been devoted to the study of the martensitic transformation, the shape memory effect, and the superelasticity of these alloys.[4–10] Many articles describe the mechanical behaviors of NiTi alloys mainly concerning plastic deformation.[11,12] Few studies were found to be devoted to the fracture behavior of NiTi alloy such as that reported by Gall *et al.*[13] In that work, the mechanism of fracture was identified as being due to (1) nucleation, growth, and coalescence of voids from Ti_3Ni_4 precipitates; and (2) cleavage fracture on {100}. Cleavage fracture was found to act in conjunction with ductile tearing.

Based on observations of *in-situ* tensile tests and detailed analysis of fracture surfaces, this work aims at the fracture mechanism and the factors affecting the fracture process of NiTi alloy.

II. EXPERIMENTAL

A. *Materials*

A commercial binary NiTi alloy with 50.7 at. pct Ni was used, the compositions of which are shown in Table I. Specimens were 1.5, 2, and 4 mm in thickness. The vacuum-melted, forged, and rolled sheets were then heated to 800 °C for 15 minutes, ice water quenched, and aged at 500 °C for 25 minutes (1.5- and 2.0-mm sheets) and 30 minutes (4-mm sheet).

The microstructures of the aged NiTi sheets were examined as B2 and shown in Figure 1(a), with their X-ray diffraction (XRD) diagram shown in Figure 1(b). The sheets were uniform throughout, regardless of the thickness. No texture microstructures were found in the specimens. However, the lamellae-like substructures in the grains looked like martensite lamellae. The XRD diagram (Figure 1(b)) showed a small amount of martensite (B19′), which may have been produced during specimen preparation. The differential scanning calorimetry (DSC) curves for the three sheets are shown in Figure 2. The DSC heating rate for all specimens was 10 °C/min. The measured data of the critical temperatures of phase transformations for sheets are summarized in Table II. The difference in the critical temperatures of phase transformations for the specimens with various thicknesses was considered to be caused by minor variation in heat treatment. The variation of heat treatments resulted in various amounts of Ti_3Ni_4 precipitate, which affected the composition of the B2 phase and then the phase transformation temperature.

B. *Specimens*

Figure 3 shows the dimensions of specimens for *in-situ* observation of tensile tests *via* scanning electron microscopy (SEM). The detailed geometric parameters are shown in Table III. Figure 4 shows the dimensions of specimens for macroscopic tensile tests. Figure 5 shows the dimensions of specimens with narrow slit notch (II type) for three-point bending (3 PB) tests and with single or double V notches for four-point bending (4 PB) tests.

C. *Macroscopic Tensile Tests*

Tensile tests were carried out with a SHIMADZU-10TA (Japan) universal tester at a crosshead speed of 0.1 mm/min at room temperature. Applied loads and displacements were recorded and the charts converted to engineering stress and strain curves.

In loading-unloading tests, specimens were loaded to the desired applied loads, and then unloaded at the same rate

J.H. CHEN and G.Z. WANG, Professors, and W. SUN, Postgraduate Student, are with the Key State Laboratory for New Materials of Non-Ferrous Alloys, Lanzhou University of Technology, Lanzhou, Gansu, 730050, P.R. China. Contact e-mail: zchen@lut.cn

Manuscript submitted August 11, 2004.

Table I. Composition of NiTi Alloy (Weight Percent)

Ni	C	O	H	Ti
55.8	≤0.08	≤0.05	≤0.08	balance

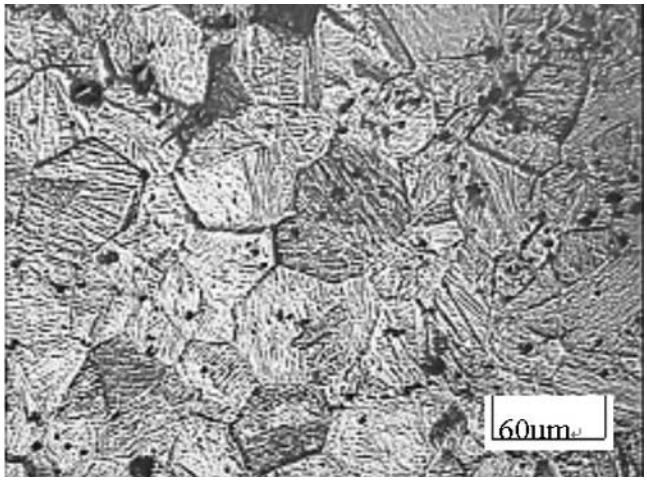

(*a*)

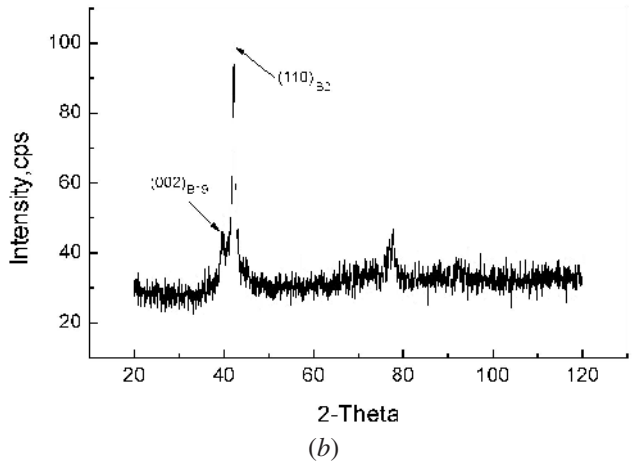

(*b*)

Fig. 1—(*a*) Microstructure of NiTi alloy and (*b*) XRD diagram.

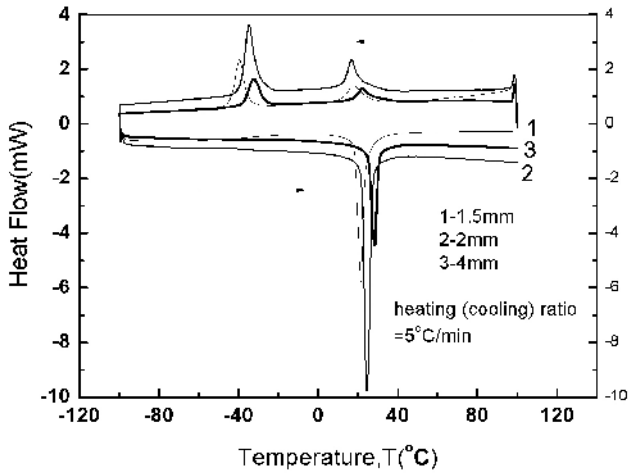

Fig. 2—DSC curves for three sheets.

Table II. Critical Temperatures of Phase Transformation (°C)

Thickness	R_s	R_f	M_s	M_f	A_s	A_f
1.5	26.03	12.10	−34.96	−43.97	18.33	23.98
2.0	21.63	12.81	−29.92	−38.85	21.96	27.29
4.0	28.47	17.3	−26.63	−37.61	21.07	30.45

R_s is the temperature of starting *R*-phase transformation in cooling, R_f the temperature of finishing *R*-phase transformation in cooling, M_s the temperature of starting martensitic transformation in cooling, M_f the temperature of finishing martensitic transformation in cooling, A_s the temperature of starting austenitic transformation in heating, and A_f the temperature of finishing anstenitic transformation in heating.

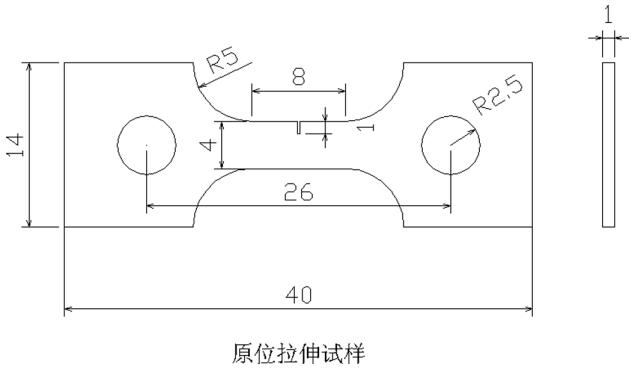

Fig. 3—Nominal dimensions of tensile specimen for *in-situ* observation *via* SEM.

as the loading processes. The loads and displacements were recorded during both processes and the measured values were converted to stress and strain data.

D. *In-Situ Tensile Tests via SEM*

In-situ tensile tests were performed in a vacuum using a calibrated load-controlled stage installed in a scanning electron microscope (SEM) S-520. The specimens were slowly step-loaded manually and the crack patterns were recorded by SEM at various loading steps. The processes of crack initiation and propagation were recorded in conjunction with applied loads.

E. *Fracture Surface Observations*

Fracture surface observations were carried out along the path of the surface crack extension that was recorded in the *in-situ* observation. By measuring the distances from the notch root to the designated sections of cracks on the surface of an *in-situ* tensile specimen, and measuring the distance from the notch root to designated fracture facets on the fracture surfaces of the same specimen, the fracture facets could be related in a one-to-one fashion to the sections of surface crack.

F. *3 PB and 4 PB Tests*

The 3 PB and 4 PB tests were carried out using a SHIMADZU-10TA universal tester at a crosshead speed of 0.1 mm/min. Applied loads and displacements were recorded. Fracture surfaces were observed.

Table III. Parameters of Specimens for *In-Situ* Observation of Tensile Tests *via* SEM

Number	Notch Type	ρ (μm)	d (mm)	t (mm)	w (mm)	A (mm^2)	L (mm)
401	II	87	2.0	0.48	5.96	1.901	38.98
406	II	87	2.0	0.48	5.97	1.906	38.98
203	V	240	2.0	0.87	5.94	3.428	38.95
1.501	V	250	2.0	0.375	5.96	1.485	38.95

II is straight blank notch, V v-type notch, ρ radius of notch root, d depth of notch, t thickness of specimen, w width of specimen, A area of ligament of specimen, and L length of specimen.

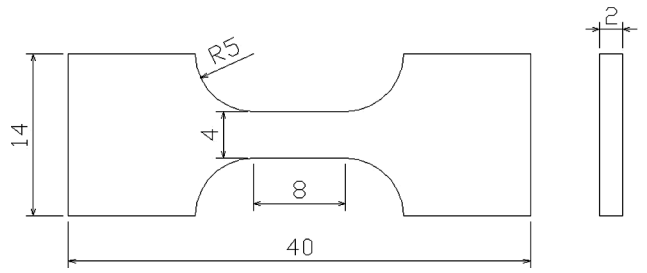

Fig. 4—Dimensions of specimen for macroscopic tensile tests.

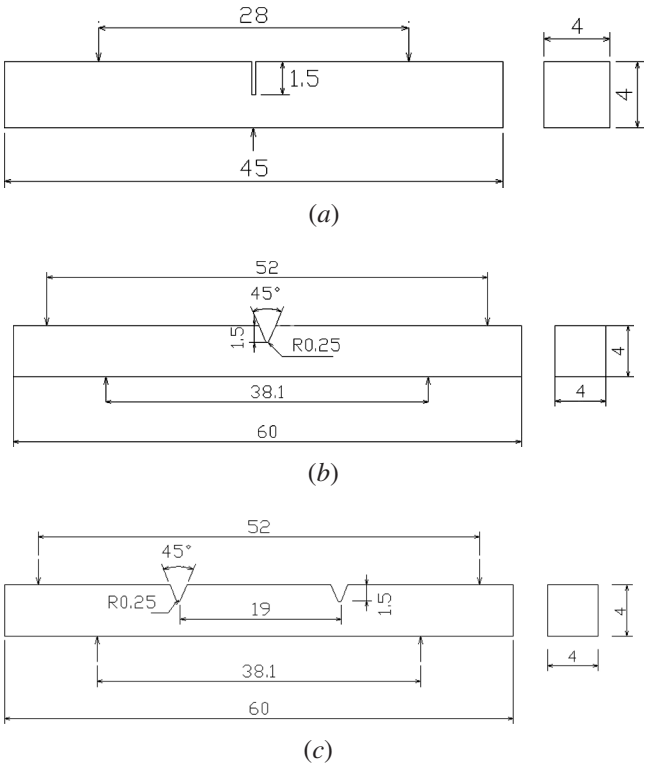

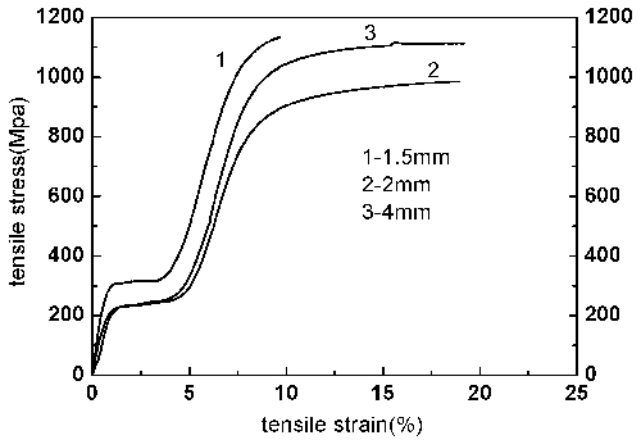

Fig. 6—Stress-strain curves of tensile tests on specimens with various thickness, line 1: 1.5 mm, line 2: 2.0 mm, and line 3: 4 mm.

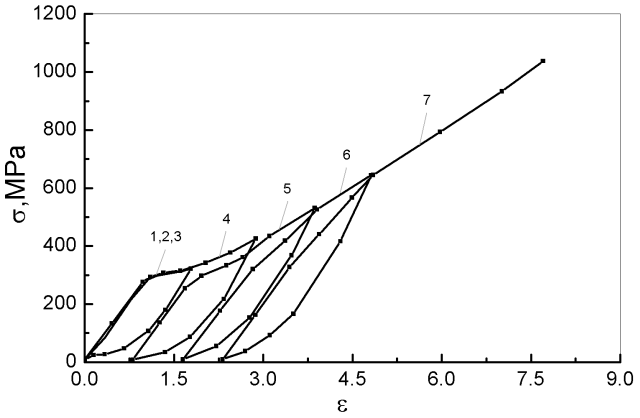

Fig. 7—Stress-strain curve for a specimen of 1.5 mm during repeated loading and unloading processes.

III. EXPERIMENT RESULTS AND ANALYSES

A. *Tensile Tests*

Figure 6 shows the stress-strain curves of tensile test results for specimens with three thicknesses. Similar to those described in Reference 12, all curves have four sections representing (1) the elastic deformation, (2) the stress-induced martensitic deformation (a pseudoelastic-plateau deformation until around 5 pct), (3) the postplateau deformation of oriented martensite (until 8 pct, caused by combined effects due to further transformation of residual austenite, reorientation, and detwinning of stress-induced martensite and plastic deformation), and (4) the plastic deformation. The transformation and the reorientation of stress-induced martensite increase the straining-capability of NiTi alloy. Due to its lower M_s (starting temperature of martensite transformation in cooling) and M_f (temperature of finishing martensite transformation in cooling), the specimen, which is 1.5 mm in thickness, shows a higher stress plateau (around 300 MPa) for inducing martensitic transformation and has a lower plastic strain at fracture.

Figure 7 shows a perfect superelasticity of specimen of 1.5 mm, in which the A_f of 23.98 °C (temperature of finish

austenite transformation in heating) is reached by the room temperature and the strain up to 1.5 pct accompanying the stress-induced martensitic transformation is fully recovered after the stress is released.

Figure 8 shows the stress-strain curve of specimens of 2.0 mm during the loading and unloading processes. Because the A_f (27.29 °C) is appreciably higher than room temperature, the strain accompanying the stress-induced martensitic transformation is not fully recovered after the stress is released. The retaining deformation will be fully recovered in the heating process, showing the shape memory effect.

Figure 8 shows the stress-strain curve for the three times of loading and unloading operations. The subsequent curve sections follow smoothly one by one and finally form a profile similar to that carried out by the single operation shown in Figure 7. This means that the processes happened in unloading are rebuilt in the reloading operations.

In Figure 9, the stress-strain curve of specimens of 4.0 mm during loading and unloading process shows a similar pattern to that of the 2-mm specimens. Because the A_f (30.45 °C) is higher, the recovered strain is less. The load drops observed during the reloading procedure need to be investigated further.

B. *In-Situ Observations of Tensile Tests in SEM*

From the applied load data and the pictures of crack patterns during *in-situ* tensile tests, curves of load-crack length and stress-crack length are obtained and shown in Figures 10(a) and (b) for specimen 401 of Table III. Here, the stress shown is the average stress of the remaining ligament. As shown in the figures, the applied load needed for further propagation decreases with increasing the crack length, but the average stress increases although the increment is not large.

Figures 11(a) through (h) show the consequent series of crack patterns observed during *in-situ* tensile test of specimen 401 with a narrow slit notch of 87 μm in width. The following events are visible.

The root of the original slit notch is shown in Figure 11(a). A crack is initiated at the notch root, and trans-grain-propagated to a short distance, it is shown in Figure 11(b).

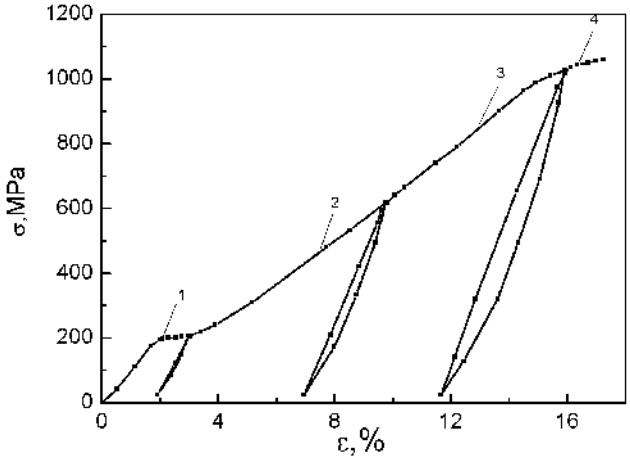

Fig. 8—Stress-strain curve for a specimen of 2.0 mm during repeated loading and unloading processes.

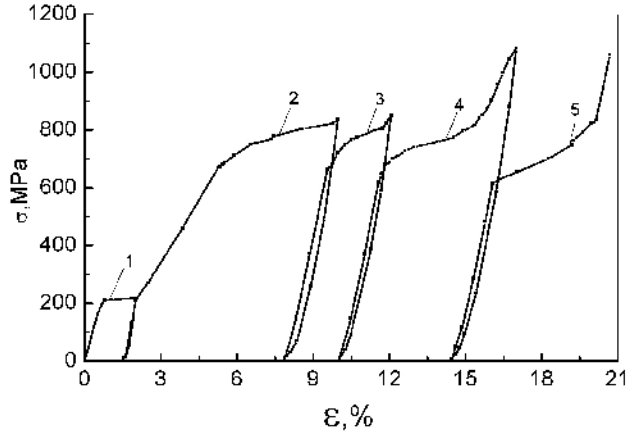

Fig. 9—Stress-strain curve for a specimen of 4.0 mm during repeatedly loading and unloading processes.

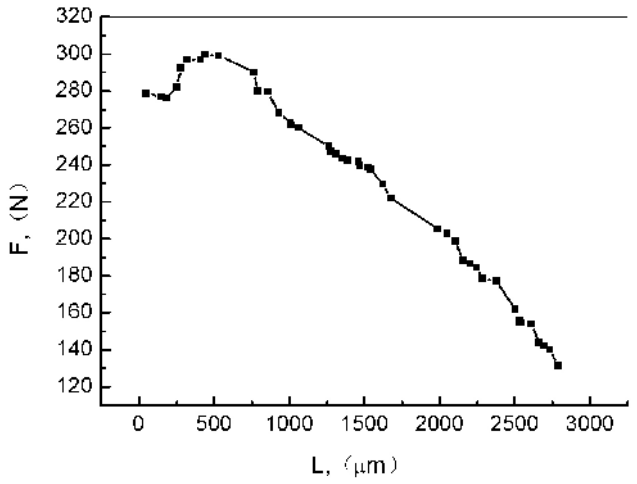

(*a*)

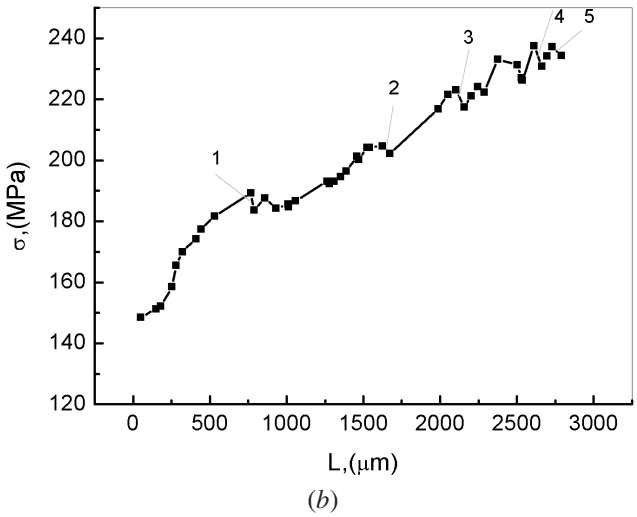

(*b*)

Fig. 10—(*a*) Applied load and (*b*) stress plotted against crack length during *in-situ* observation of a tensile test of specimen 4 mm.

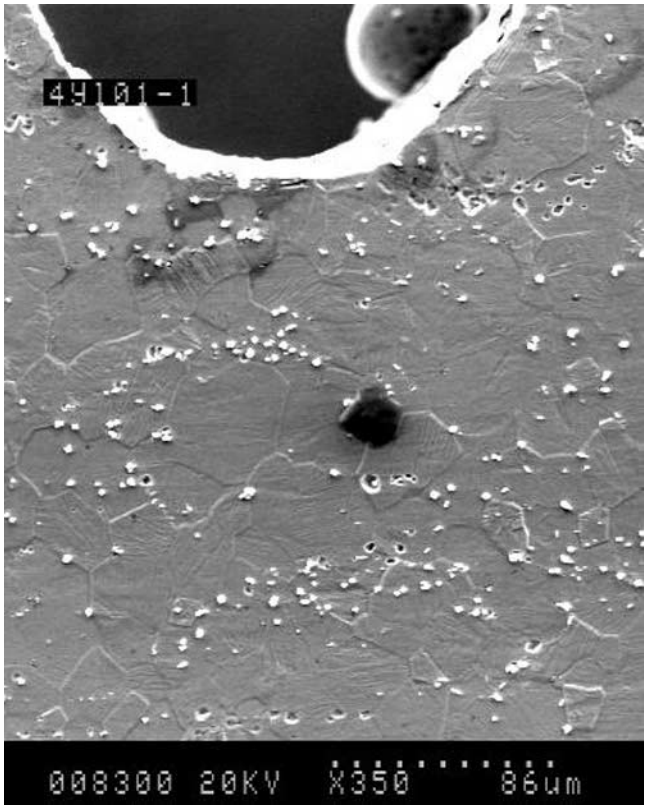

(*a*)

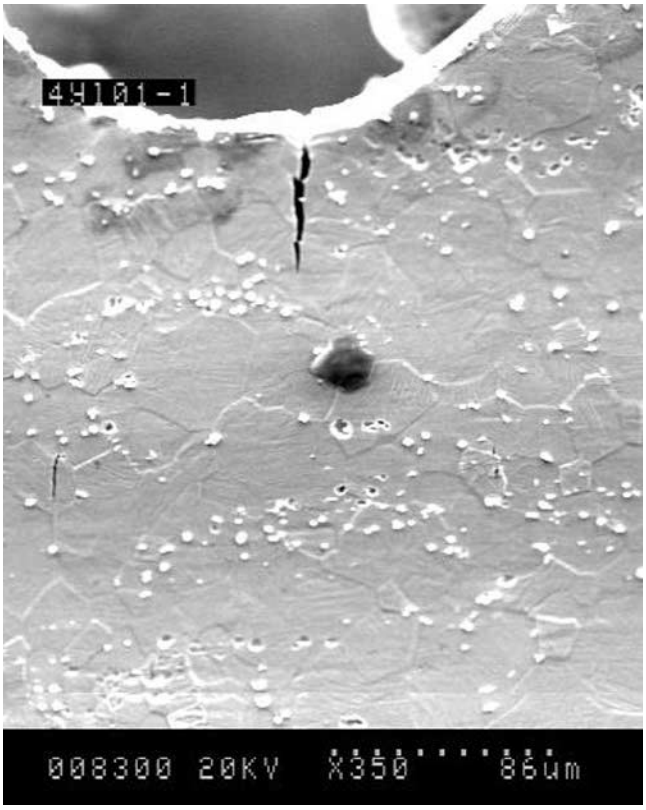

(*b*)

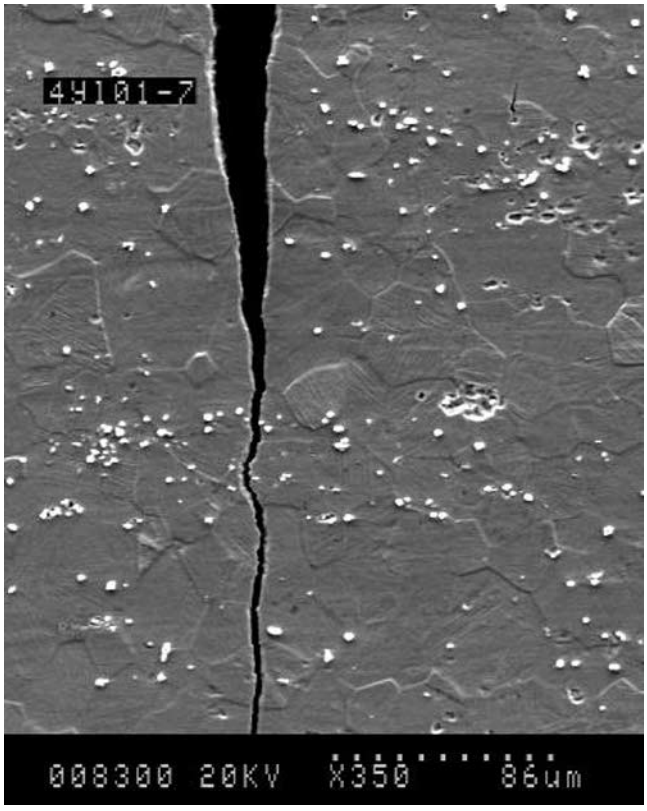

(*c*)

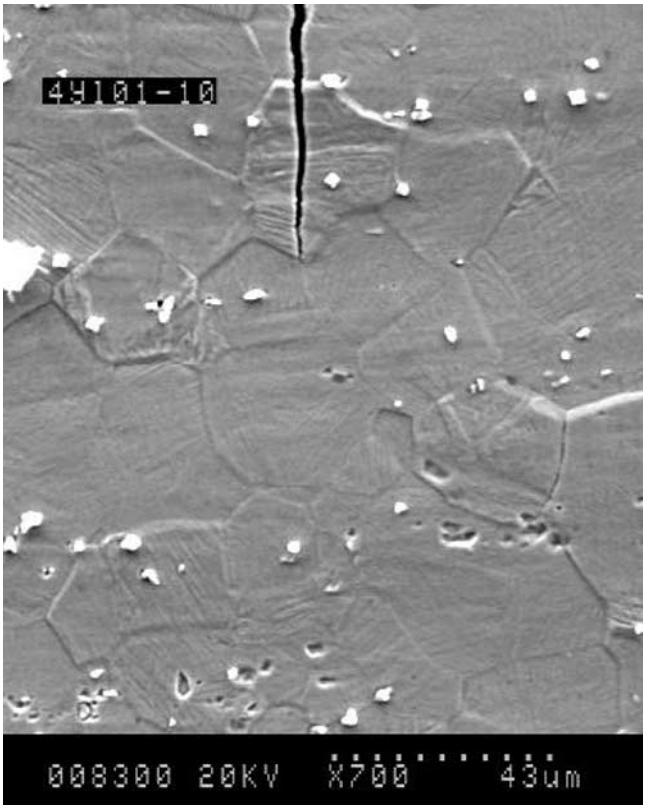

(*d*)

Fig. 11—A series of crack patterns observed in *in-situ* tensile test of specimen 401 with narrow straight notch 87 μm in root radius: (*a*) 249.33N, (*b*) 278.67N, (*c*) 297.02N, (*d*) 270.96N, (*e*) 260.48N, (*f*) 247.42N, (*g*) 242.82N, (*h*) 242.45N, (*i*) 241.74N, and (*j*) 158.74N.

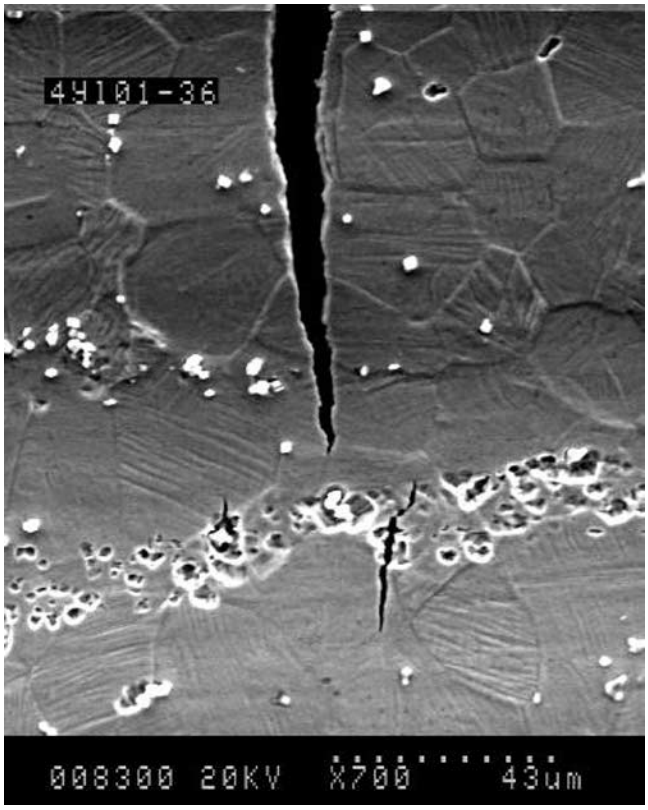

(*e*)

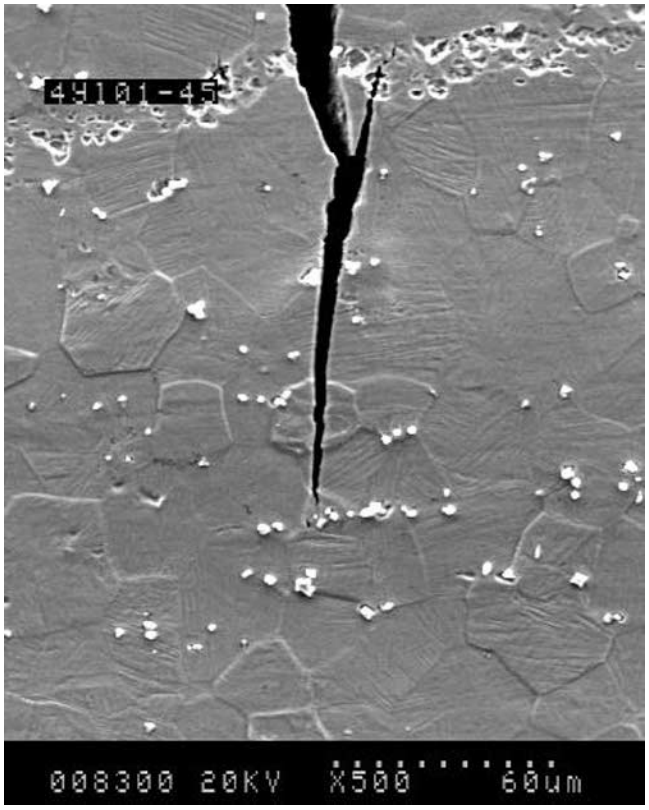

(*f*)

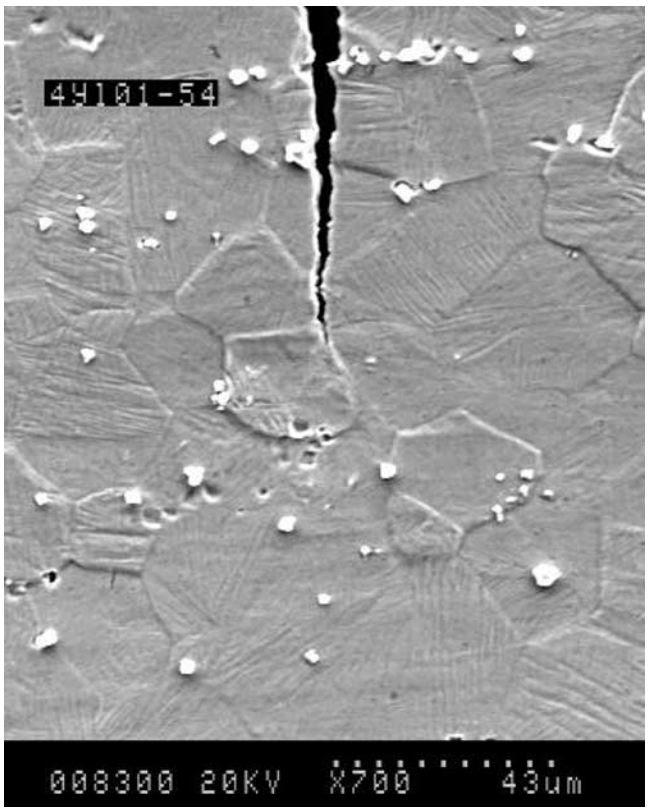

(*g*)

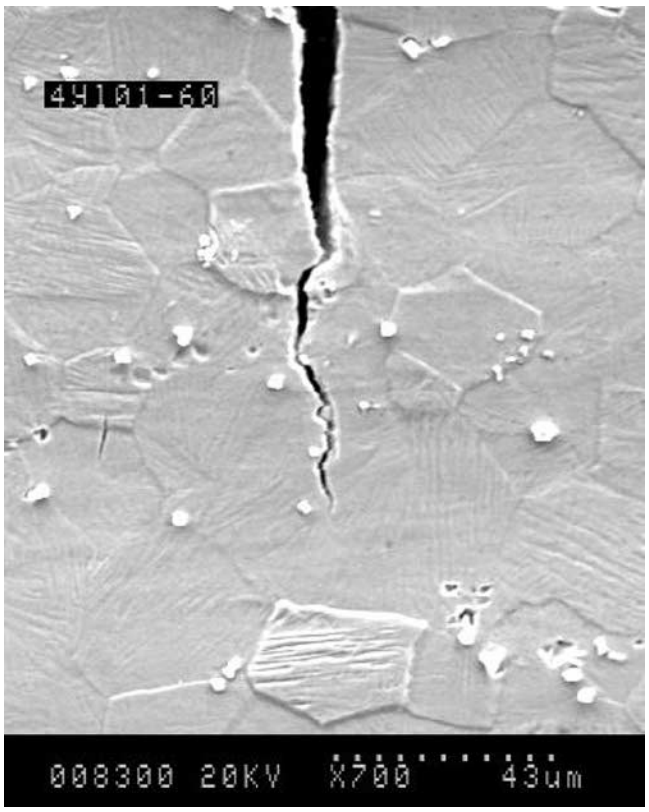

(*h*)

Fig. 11—(Continued). A series of crack patterns observed in *in-situ* tensile test of specimen 401 with narrow straight notch 87 μm in root radius: (*a*) 249.33N, (*b*) 278.67N, (*c*) 297.02N, (*d*) 270.96N, (*e*) 260.48N, (*f*) 247.42N, (*g*) 242.82N, (*h*) 242.45N, (*i*) 241.74N, and (*j*) 158.74N.

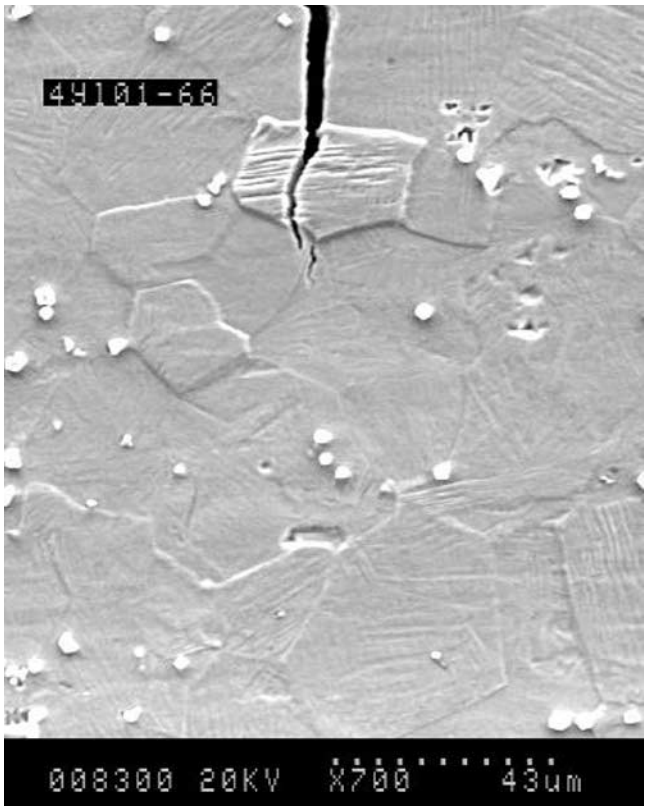

(*i*)

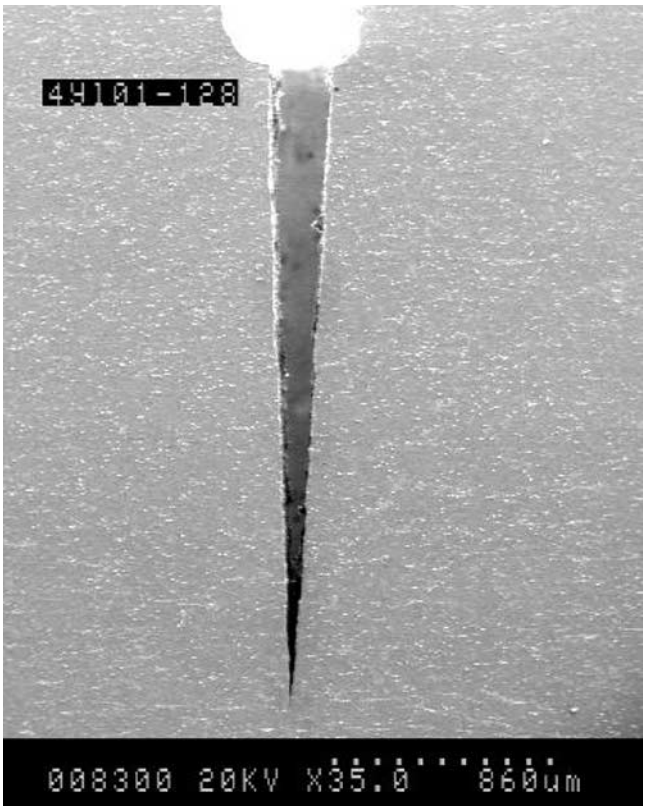

(*j*)

Fig. 11—(Continued). A series of crack patterns observed in *in-situ* tensile test of specimen 401 with narrow straight notch 87 μm in root radius: (*a*) 249.33N, (*b*) 278.67N, (*c*) 297.02N, (*d*) 270.96N, (*e*) 260.48N, (*f*) 247.42N, (*g*) 242.82N, (*h*) 242.45N, (*i*) 241.74N, and (*j*) 158.74N.

The crack is propagated in line with the maximum normal stress and bypasses the white second phase (Ti_3Ni_4) particles (Figure 11(c)). Sometimes the crack propagates unstably through a region with coarse microsubstructure. The crack is trans-lamellar-propagated through a grain (Figure 11(d)). The direction of lamellae seems to have little effect on the propagation. Figures 11(e) and (f) show that a crack is initiated in a band of cavities left by erased second-phase particles and finally connects with the main crack. Figures 11(g) and (h) show that the crack does not prefer to propagate through the grain boundary. The crack remains in line with the maximum normal stress even though some twists occur on the way. Figure 11(i) shows a crack initiated at a junction of three grains. Figure 11(j) shows a general view of a crack, which extends to around 2.5 mm and remains in line with the maximum normal stress. A fracture throughout the remaining ligament is triggered at a crack length around 3.5 mm.

An analysis of the fracture mechanism is as follows. The main crack is initiated at the notch tip and propagates in line with the direction of the maximum normal stress showing a strong stress-controlling mode of crack propagation. It is well known that the tensile stress at the notch tip is much lower than the maximum tensile stress produced by stress intensification at a distance ahead of the notch tip. The higher the applied load, the higher the tensile stress in a notched specimen. The fact that main crack is initiated just at the notch root (instead of at a distance ahead of the notch tip) and at a low applied load means the local fracture stress of NiTi alloy is very low. From Figure 10(b), the stress that initiated the crack is lower than 200 MPa $\times$ 1.15 = 230 MPa $<$ 250 MPa.

Figure 12 shows two short white strips developing at the crack tip in directions of 45 deg inclining toward the direction of maximum normal stress in specimen 406. This is considered to be the reflection of Luderslike deformation associated with stress-induced martensitic transformation in NiTi. Due to the high stress and heavy strain developed in front of an appreciably blunted crack tip, martensite is induced before the crack propagated further. The produced pseudoelastic plateaus in Figure 6 create extra strain to blunt the crack tip. The width of the blunted main crack tip in specimen 406 is appreciably wider than that of specimen 401.

The grain orientation, lamellae orientation (Figure 11(d)), and grain boundaries (Figures 11(g) and (h)) show little effect on the direction of crack propagation. The isotropic behavior of the NiTi alloy is unusual for intermetallic compounds and is considered to result from the dominant effect of the martensitic transformation. The martensite transformation induced by the high stress and the strain ahead of the crack tip produced appreciable additional strains, which make the fracture a quasi-cleavage pattern rather than a cleavage one. The crack propagates in the martensite, which has been transformed from the existing phase. This process makes the originally existing microstructure insignificant to crack propagation.

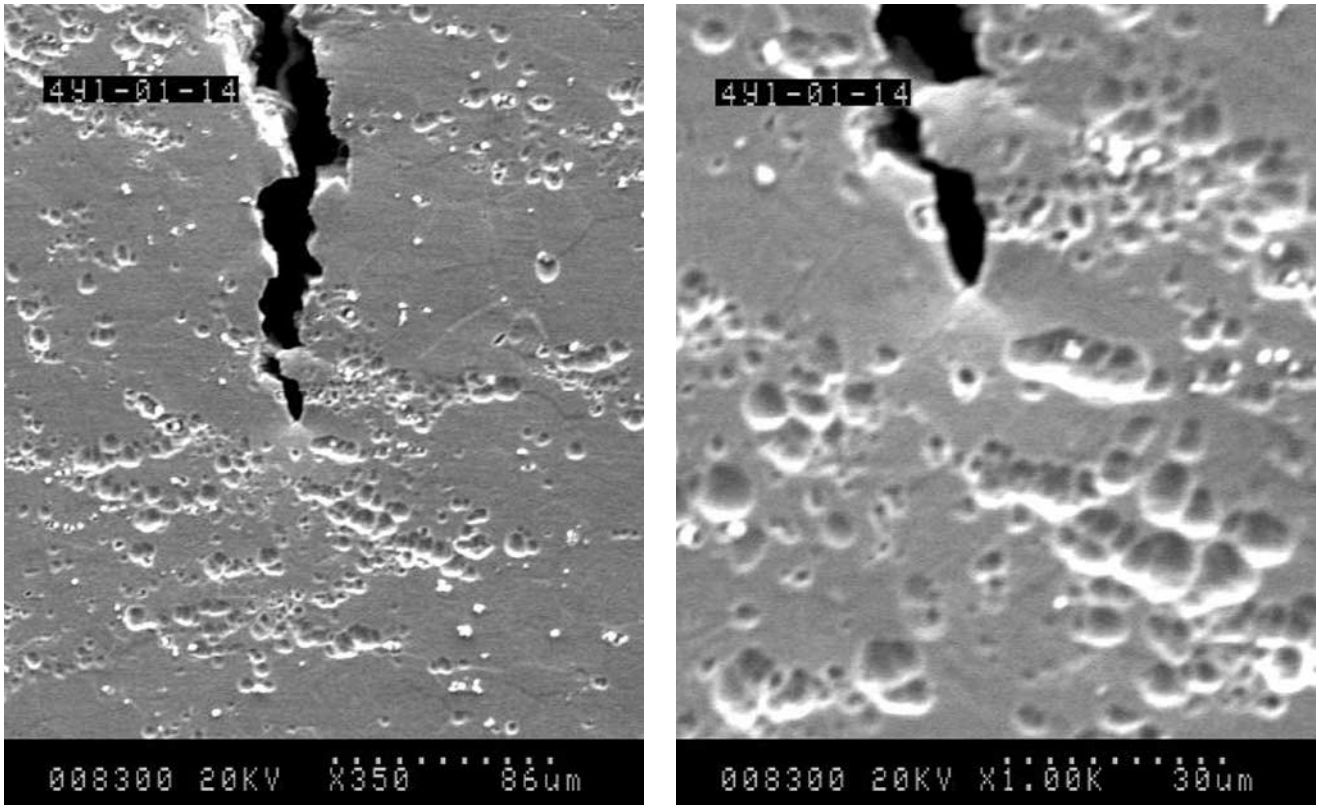

(*a*) (*b*)

Fig. 12—Luderslike deformation developed in front of a crack tip: (*a*) 442.22N and (*b*) 442.22N.

In a few cases, microcracks can be initiated at the junction of three grains (Figure 11(i)) where the incompatibility of deformation causes higher stress concentration and stress triaxiality.

The second-phase particles (Ti_3Ni_4) have higher resistance to crack propagation and make detours for the main crack (Figure 11(c)), but in some cases, microcracks can be initiated under the effect of second-phase particles (Figures 11(e) and (f))

Figure 13 shows the crack pattern produced during the *in-situ* tensile test of a specimen of 2 mm with V notch of 270 μm in root radius. The main crack is also initiated at the notch root and propagated directly from it. However, many microcracks are produced in the vicinity of the notch root. The specimen is suddenly fractured after the main crack propagates a very short distance.

Figure 14(a) shows a similar case for a specimen of 1.5 mm. In this specimen, instead of many microcracks, only one crack is initiated and propagated close to the main crack.

The different cracking behaviors presented in the preceding specimens are considered to be caused by different acuities of the notch root. In the narrow slit-notched specimen, the stress intensification is higher. The crack is initiated at lower applied loads, propagates step-by-step, and is controlled by stress (Figure 10). In V-notched specimens, the crack is initiated and propagates a short distance at higher applied loads and higher average stress, as shown in Figures 14(c) and (d), which are sufficient to trigger fracture over all specimens. The similar trend is observed in bending tests.

C. *Bending Tests*

Figure 15 shows load-displacement curves for the 3 PB test of a specimen with a narrow slit notch, the 4 PB test of V-notch specimen, and the 4 PB test of double V-notch specimen. Specimens are cut from 4-mm NiTi sheet. Due to the different spans between the points of loading and reactions, the values of applied loads are incomparable, but the curves show a similar trend as in the *in-situ* tensile tests. For the specimen with a narrow slit notch, the trend of load-displacement curve looks like that shown in Figure 10(a). It implies that a crack is produced at a low applied load and propagates to a long distance before final fracture. For specimens with V-notch, the trends of load-displacement curves look like that shown in Figure 13(c). As analyzed previously, the different fracture behaviors are considered to be caused by different acuities in the notch root. In a narrow slit notch specimen, the higher stress at the notch root is sufficient to initiate a crack at a low applied load, at which the accumulated elastic energy is insufficient to cause an overall fracture and the crack is propagated step by step. In a V-notch specimen with a wider root, the crack is initiated at a higher applied load at which the accumulated energy is sufficient to cause an overall fracture after a short extension of the crack.

It seems that a narrow slit notch of 87 μm in width is too acute, yet a 45 deg V-notch of 250 μm in radius is too blunt to evaluate the fracture toughness of NiTi alloy. An ideal specimen for evaluating the fracture toughness of NiTi alloy should have a notch with a blank angle between 45 and 0 deg and a root radius between 250 and 43.5 μm.

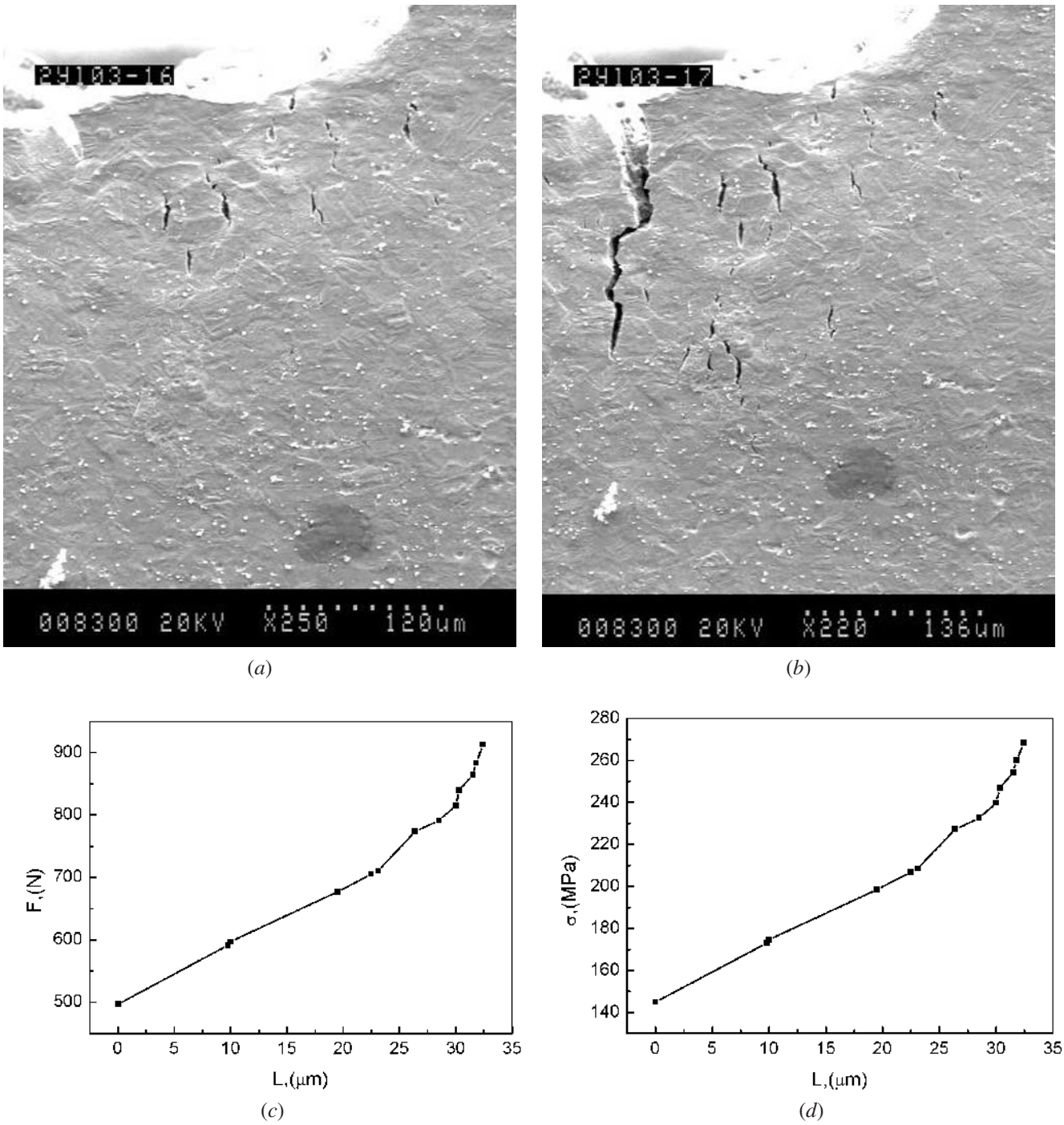

Fig. 13—The crack pattern of *in-situ* tensile test of V-notched specimen of (*a*) and (*b*) 2 mm, and (*c*) load- and (*d*) stress-crack length curves.

D. *Fracture Surfaces*

Figure 16 shows typical fracture surfaces of NiTi alloy tensile-tested at room temperature. The quasi-cleavage pattern prevails throughout the fracture surface (Figure 16(a)). Facets of cleavage (Figures 16(b) and (c)) mixed with featureless morphology are surrounded by tear ridges (white strips in Figure 16(c), which also show the brittle pattern). Many parts, especially on the left side of the fracture surface (Figures 16(a) and 17(b)), where the surface is polished and etched for observation, show lamellar facets surrounded by strip ridges. The lamellar substructure is considered to be the martensitic layers, which are produced by the polishing procedure done on the specimen's surface before the test. Due to the high A_f, the stress-induced martensite cannot be recovered at room temperature.

By measuring the distances from the notch root, the fracture facets corresponding to designated crack sections with the same distances can be found. From Figure 10, it is revealed that in the region of crack length from 200- to 450-μm crack propagation is more difficult with increments

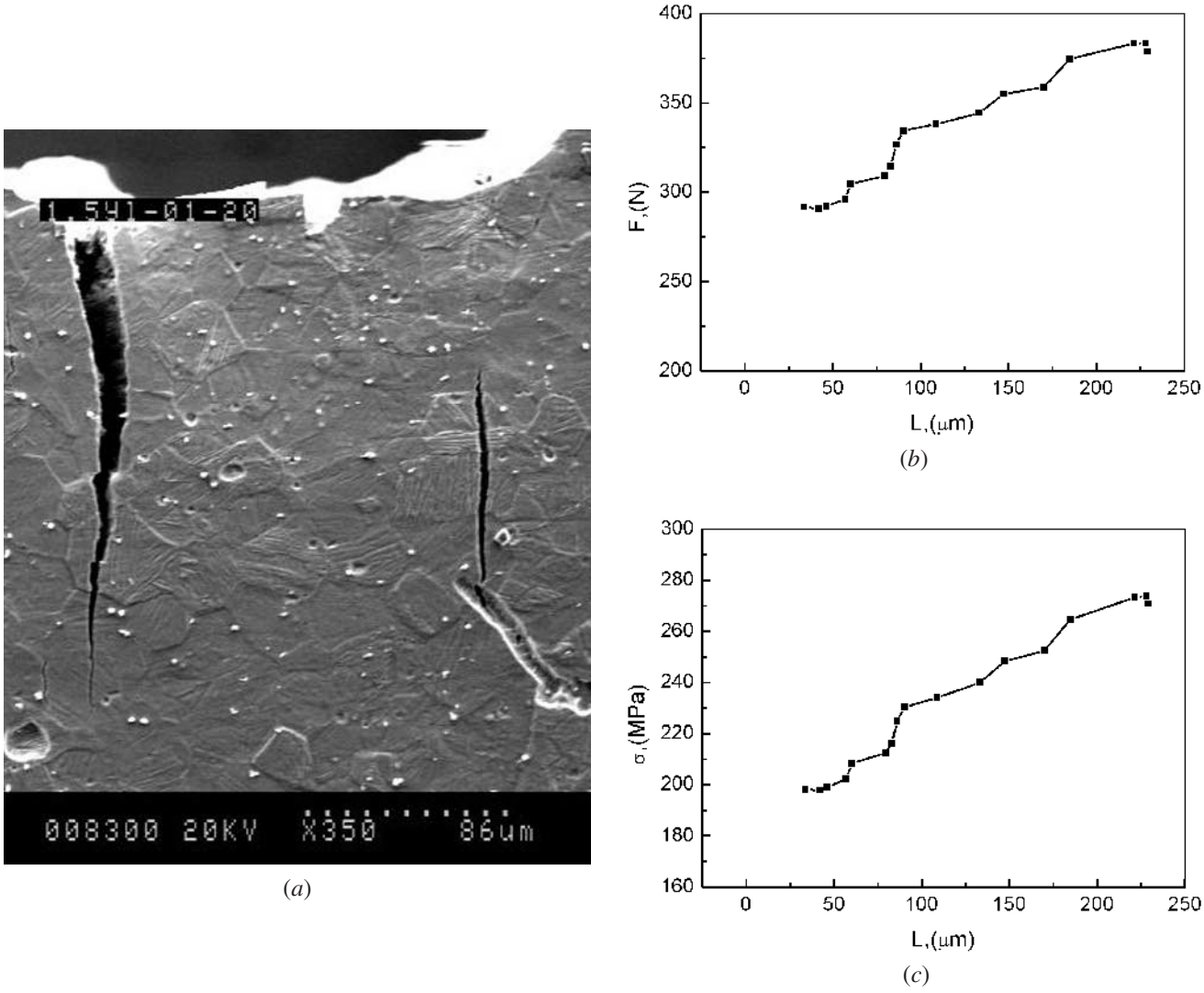

Fig. 14—The crack pattern of *in-situ* tensile test of V-notched specimen of (*a*) 1.5 mm and (*b*) load- and (*c*) stress-crack length curves. (*a*) 383.31N.

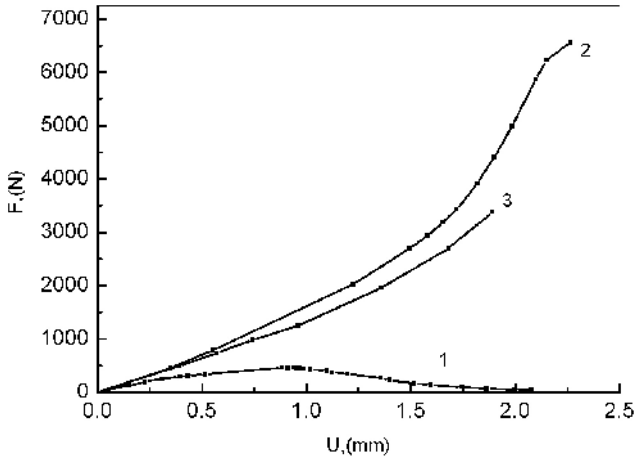

Fig. 15—Loads-displacement curve for the 3 PB test of narrow straight notch specimen line 1, 4 PB test of V-notch specimen line 2, and 4 PB test of double V-notch specimen of 4 mm line 3.

of stress more than 300 MPa. The corresponding fracture surface shows finer fracture facets (Figure 17(b)). In the region of crack length around 1800 μm, the crack propagated unstably with an increment of 500 μm at a maintained stress and caused a remarkable decrease of applied load. The corresponding fracture surface shows appreciably coarser facets (Figure 18(b)). Similar cases are observed in the crack length region around 800 and 2400 μm. Therefore, although the microstructure has little effect on the direction of crack propagation, coarser substructures show lower resistance to the crack propagation. This means that loading process factors, which cause the induced martensite layers to be finer, can improve the alloy's toughness.

Figure 19 shows the fracture surfaces of bending specimens. In general, the fracture surfaces of bending specimens show similar patterns as that of *in-situ* tensile specimens. The quasi-cleavage prevails throughout the fracture process and shows that the NiTi is not as brittle as TiAl intermetallic compounds. It is considered to result from the extra plas-

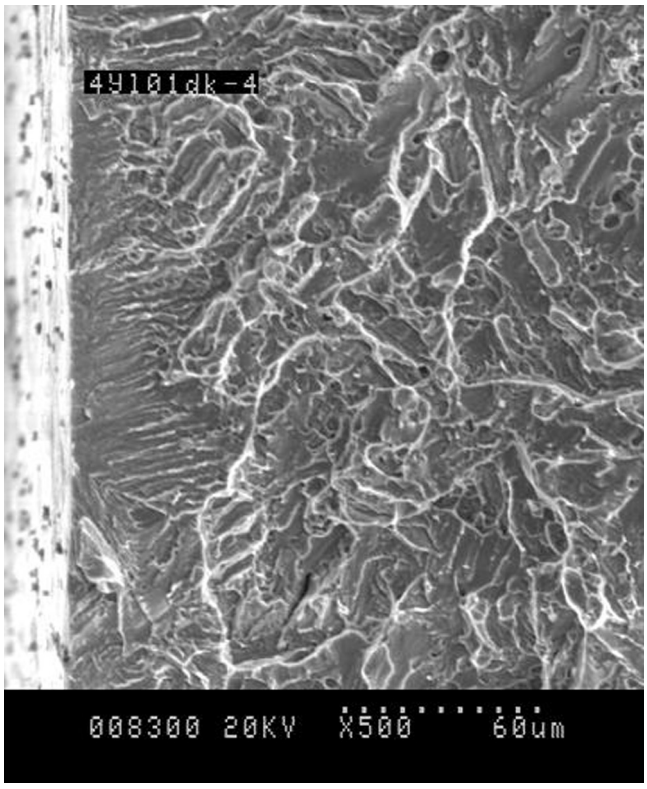

(*a*)

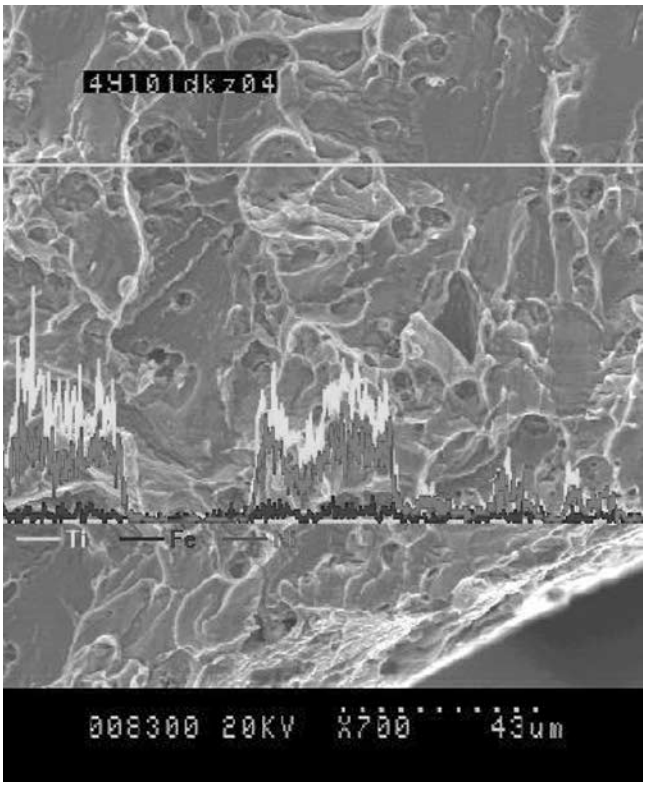

(*b*)

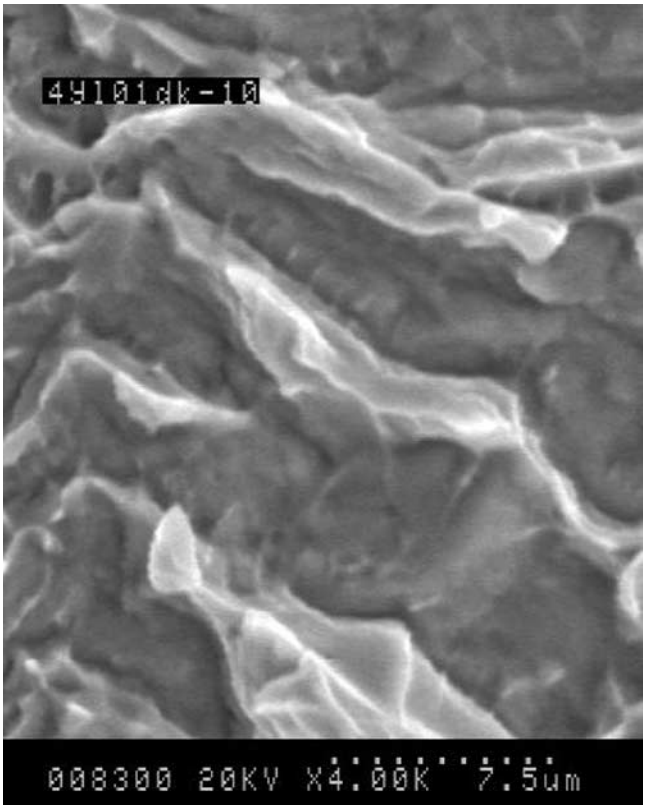

(*c*)

Fig. 16—Typical fracture surfaces of NiTi alloy tensile tested at room temperature.

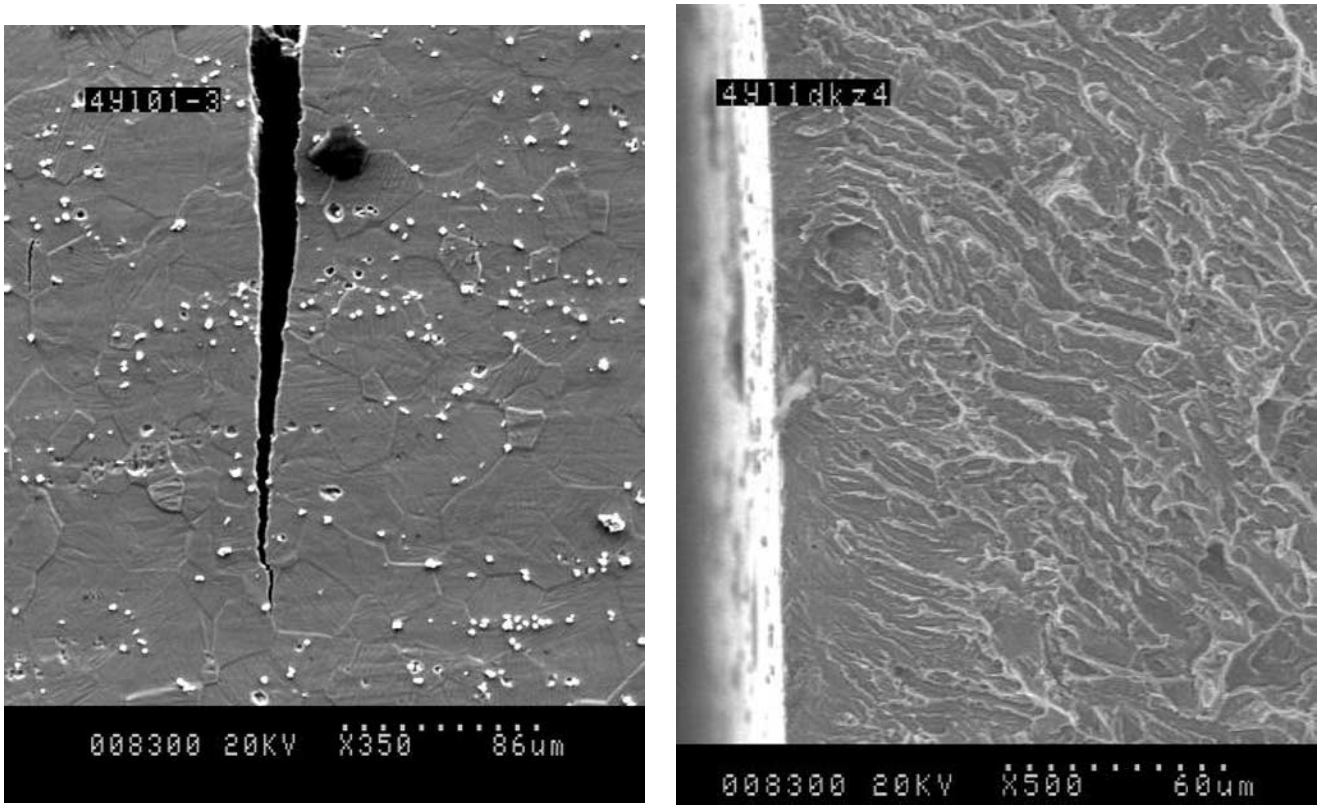

(*a*) (*b*)

Fig. 17—Crack pattern and corresponding fracture surface at crack length around 300 μm.

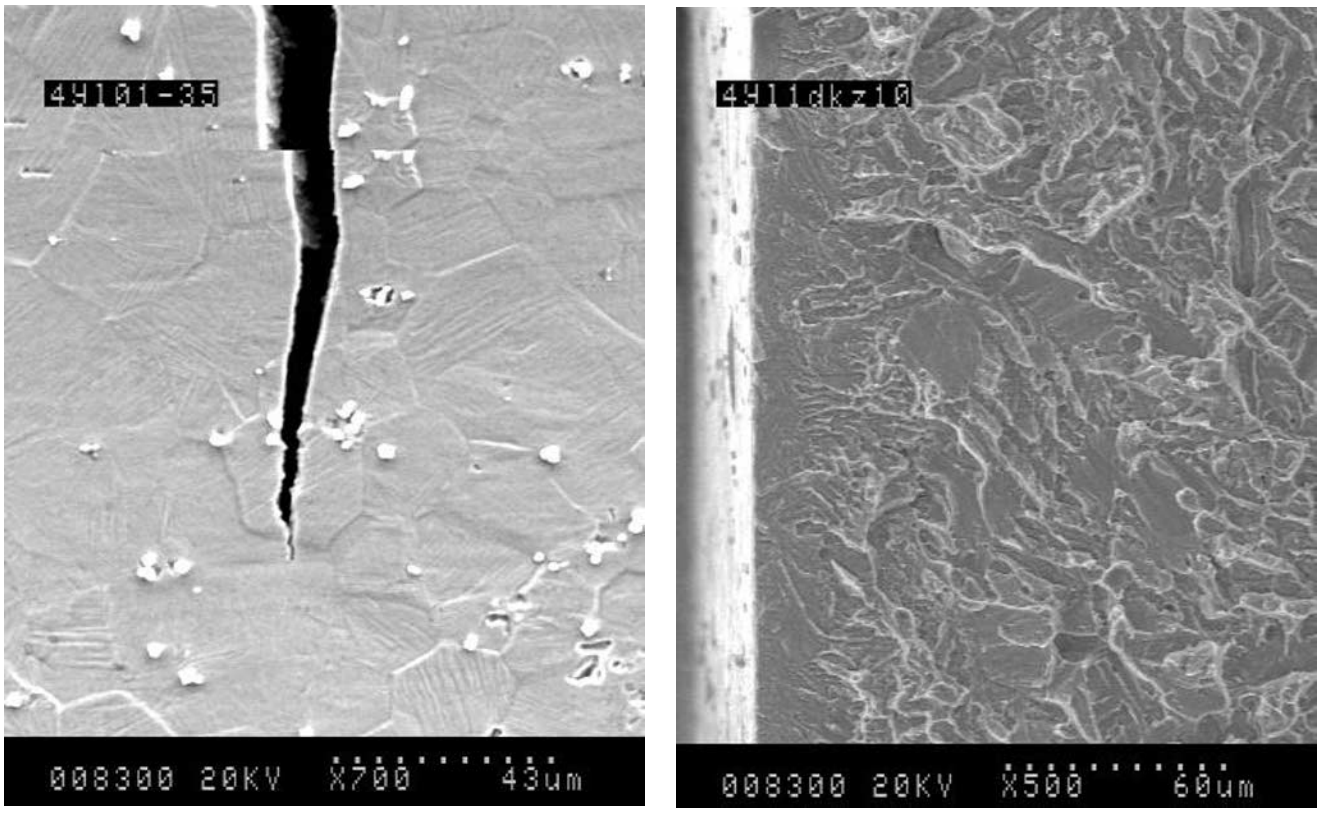

(*a*) (*b*)

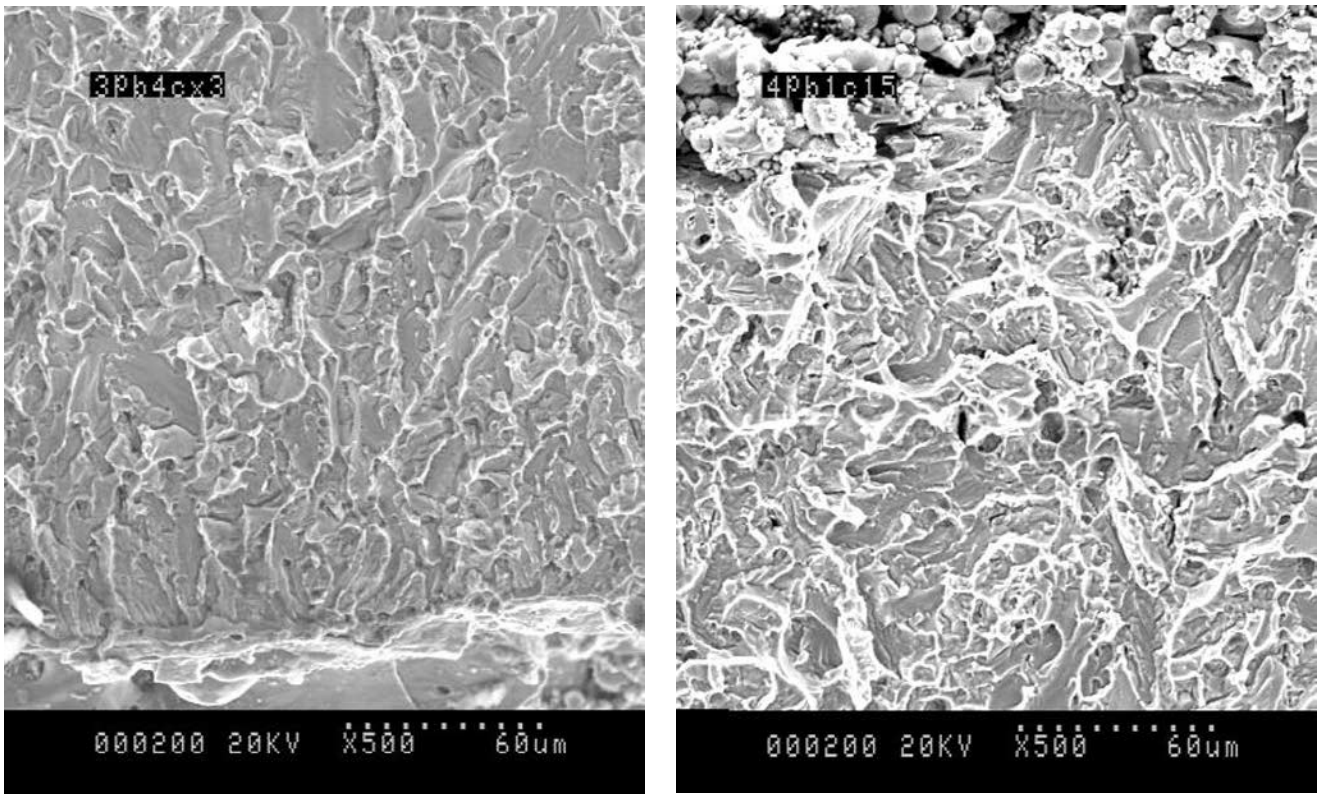

(*a*) (*b*)

Fig. 19—Fracture surface of (*a*) 3 PB testing specimen and (*b*) 4 PB testing specimen.

ticity caused by induced martensite formation. This extra plasticity offers a wider blunted crack tip and makes the featureless-morphology facets in Figure 16(c). In a coarse grain region, the crack propagates at a high rate. The plastic strain produced by crack blunting is low, the induced martensite constituent, and then the accompanying plastic strain is low. The crack shows the cleavage pattern. In a fine grain region, the crack is appreciably blunted. The produced plastic strain induces more martensite transformation and additional extra plastic strain. Finally, the crack is propagated by tearing.

Figure 20 shows a fracture surface of the smooth tensile-tested specimen of 4 mm. The fracture is initiated from one side of the specimen (bottom side in Figure 20(a)) and shows clear Chevron strips. The fracture surface (Figures 20(b) and (c)) shows a fracture pattern appreciably tougher than those observed in notched specimens. Much finer facets with the featureless and even dimplelike facets are surrounded by much denser ridges. The different fracture patterns shown by smooth specimens and by notched specimens are apparently caused by different stress triaxiality values. This means that NiTi alloy is sensitive to stress conditions.

IV. SUMMARY

Based on macroscopic mechanical tests and microscopic *in-situ* observations of tensile fracture processes via SEM in connection with analyses of the fracture surfaces, the fracture behaviors of NiTi alloy at room temperature can be summarized.

1. At room temperature, NiTi shows either a shape memory effect ($T < A_f$) or superelasticity ($T > A_f$).
2. The main crack is initiated at the notch root and is propagated in line with the direction of the maximum normal stress showing a strong stress-controlling mode of crack propagation.
3. A quasi-cleavage prevails in the fracture process of NiTi alloy. Facets of cleavage mixed with featureless morphology produced by tearing are surrounded by tear ridges. Notch acuity has an appreciable effect on the fracture pattern.
4. The microstructure has little effect on the direction of crack propagation, but coarser substructures show lower resistance to the crack propagation.
5. Microcracks can be initiated at the junction of three grains and at inclusions or second-phase particles. The initiated and extended crack is finally connected with the main crack and keeps the crack propagation in line with the direction of maximum normal stress.
6. Stress (strain) induced martensitic transformations play an important role in improving the toughness of NiTi alloy; however, this still needs further investigation.

ACKNOWLEDGMENTS

The authors express their gratitude to the Xi Mai New Materials Cooperation for offering the NiTi alloy and Miss

(*a*)

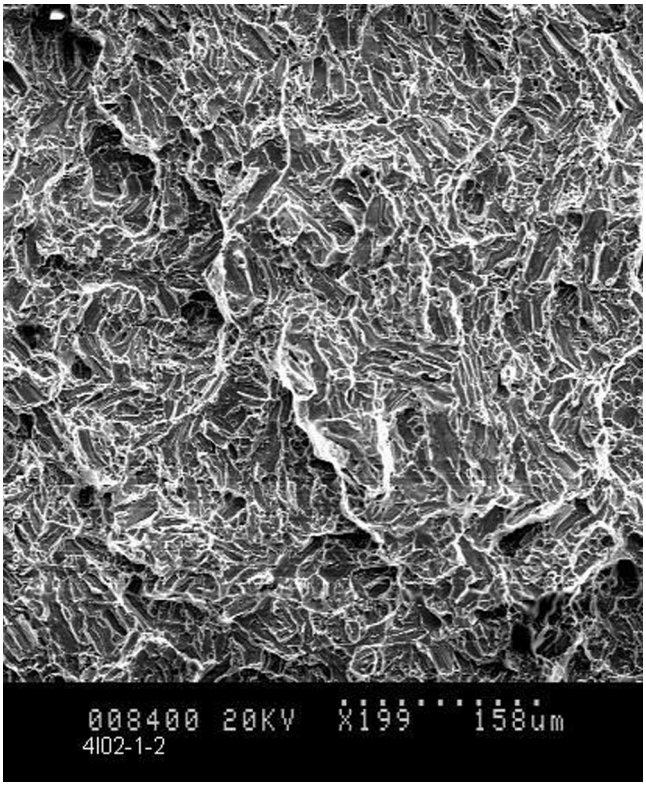

(*b*)

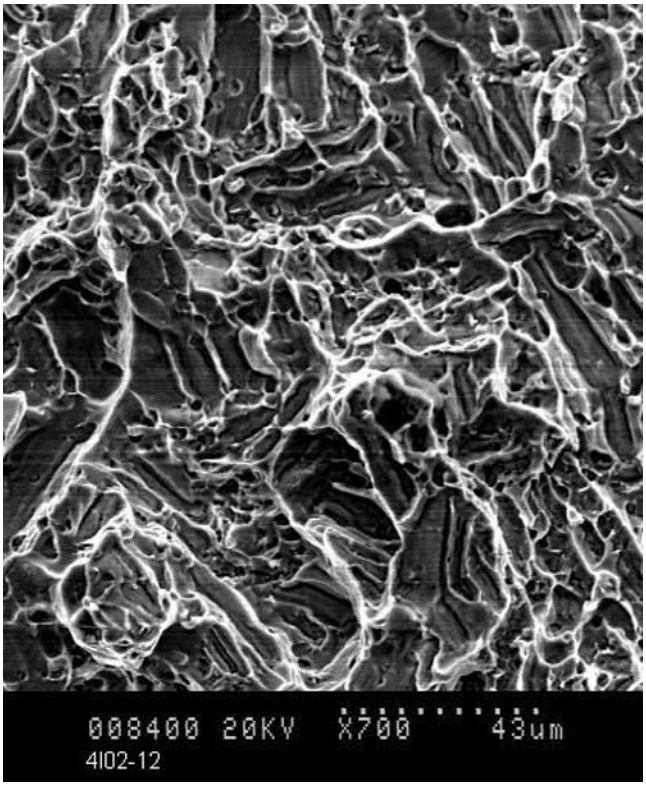

(*c*)

Fig. 20—Fracture surface of tensile tested specimen.

Cao Rui for her help in manuscript preparation. Special thanks to Miss Martha Ello for her help in literal revision.

REFERENCES

1. M. Bezzi, F. Orsi, and F.M. Salvitori: *JVIR*, 1994, vol. 5, pp. 287-93.
2. J.E. Bramfitt and R.L. Hess: *Proc. 1st Int. Conf. on Shape Memory and Superelastic Technology*, CA, 1994, pp. 435-40.
3. Y. Chu, K. Dai, and M. Zhu: *Mater. Sci. Forum*, 2000, pp. 327-28 and 55-62.
4. W.J. Wasilewski, S.R. Butler, and J.E. Hanlon: *Metall. Trans*., 1971, vol. 2, pp. 229-38.
5. S. Miyazaki, Y. Ohmi, and K. Otsuka: *J. Phys*., 1982, vol. 43 (C4), pp. 225-37.
6. C.M. Wayman, J. Cornelis, and K. Shimizu: *Scripta Metall*., 1972, vol. 6, pp. 115-22.
7. G.B. Stachowiak and P.G. Mccormick: *Acta Metall*., 1988, vol. 36, pp. 291-96.
8. T. Saburi: *Shape Memory Materials*, Cambridge University Press, Cambridge, United Kingdom, 1998, p. 77.
9. L. Tan and W.C. Crone: *Scripta Mater*., 2004, vol. 50, pp. 819-23.
10. T. Waitz, V. Kazykhanov, and H.P. Karnthaler: *Acta Mater*., 2004, pp. 137-47.
11. S. Miyazaki and K. Otsuka: *Phil. Mag. A*, 1984, vol. 50, pp. 393-408.
12. G. Tan, Y. Liu, P. Sittner, and M. Saunders: *Scripta Mater*., 2004, vol. 50, pp. 193-98.
13. K. Gall, N. Yang, H. Sehitoglu, and Y.I. Chumlyakov: *Int. J. Fract*., 2001, vol. 109 pp. 189-207.